NeuroImage 163 (2017) 13–23

Contents lists available at ScienceDirect

NeuroImage

journal homepage: www.elsevier.com/locate/neuroimage

The impact of vessel size, orientation and intravascular contribution on the neurovascular fingerprint of BOLD bSSFP fMRI

Mario Gilberto Báez-Yánez [a,b], Philipp Ehses [a,c], Christian Mirkes [a,d], Philbert S. Tsai [e], David Kleinfeld [e,f], Klaus Scheffler [a,g,*]

[a] Department of High-Field Magnetic Resonance, Max Planck Institute for Biological Cybernetics, Tuebingen, Germany
[b] Graduate Training Centre of Neuroscience, University of Tuebingen, Tuebingen, Germany
[c] German Center for Neurodegenerative Diseases (DZNE), Bonn, Germany
[d] Skope Magnetic Resonance Technologies, Zurich, Switzerland
[e] Department of Physics, University of California at San Diego, La Jolla, CA, USA
[f] Section of Neurobiology, University of California, La Jolla, CA, USA
[g] Department of Biomedical Magnetic Resonance, University of Tuebingen, Tuebingen, Germany

ARTICLE INFO

Keywords:
Vascular cortical network
Layer specific BOLD fMRI
Orientation-dependent BOLD fMRI
Extra- and intravascular contribution
Balanced SSFP

ABSTRACT

Monte Carlo simulations have been used to analyze oxygenation-related signal changes in pass-band balanced steady state free precession (bSSFP) as well as in gradient echo (GE) and spin echo (SE) sequences. Signal changes were calculated for artificial cylinders and neurovascular networks acquired from the mouse parietal cortex by two-photon laser scanning microscopy at 1 μm isotropic resolution. Signal changes as a function of vessel size, blood volume, vessel orientation to the main magnetic field B_0 as well as relations of intra- and extravascular and of micro- and macrovascular contributions have been analyzed. The results show that bSSFP is highly sensitive to extravascular and microvascular components. Furthermore, GE and bSSFP, and to a lesser extent SE, exhibit a strong dependence of their signal change on the orientation of the vessel network to B_0.

1. Introduction

The signal-to noise ratio of the MR signal increases more than linear with field strength (Ocali and Atalar, 1998; Wiesinger et al., 2004), and an increase with a power of about 1.7 was recently reported for brain imaging between 3T and 9.4T (Pohmann et al., 2016). Imaging at 7T or 9.4T therefore opens the possibility to resolve structures far below the thickness of 2–3 mm of the human neurocortex. Anatomical images with an isotropic resolution below 200 μm have been obtained at 9.4T (Budde et al., 2014a, 2014b; Lüsebrink et al., 2017) that clearly resolve subcortical structures such as the line of Gennari or subcortical units within the brain stem (Federau and Gallichan, 2016; Keuken et al., 2013; Deistung et al., 2013). Functional images based on the blood oxygenation level dependent (BOLD) effect and acquired with gradient echo or spin echo methods, in principle, may offer the same spatial resolution as anatomical images. Therefore, at very high fields the BOLD response from single cortical layers or other mesoscopic substructures might be resolved. However, while the spatial point-spread-function in structural images is basically given by a *sinc* function with a width given by the inverse of the sampled k-space coverage, in functional BOLD imaging the neurovascular point-spread-function defines the resolution of a point-like neuronal event that is blurred by vascular-related changes related to tissue oxygenation, blood flow and blood volume.

So far, MR imaging is only able to detect vascular-related changes triggered by neuronal events or other physiological changes, like vasomotion (Murphy et al., 2013). Observed signal changes related to changing blood oxygenation levels within the neurovascular network depend on the chosen imaging modality. For example, it is well-known that spin echoes are selective to oxygenation changes from only small vessels in the range of 5–20 μm, whereas gradient echoes are sensitive to all vessel calibers larger than about 5 μm (Weisskoff et al., 1994; Boxerman et al., 1995). Furthermore, the neurovascular system is not a randomly oriented network of micro vessels but has a distinct geometry of surface vessels that are oriented parallel and penetrating vessels that are oriented perpendicular to the cortex surface (Weber et al., 2008; Blinder et al., 2013). Thus the orientation of the cortex to the main magnetic field might significantly influence the detected BOLD signal (Gagnon et al., 2015).

* Corresponding author. MPI for biological Cybernetics, Spemannstrasse 41, 72076, Tübingen, Germany.
E-mail address: klaus.scheffler@tuebingen.mpg.de (K. Scheffler).

http://dx.doi.org/10.1016/j.neuroimage.2017.09.015
Received 16 May 2017; Received in revised form 17 August 2017; Accepted 6 September 2017
Available online 8 September 2017

The susceptibility difference between (partially) deoxygenated blood and surrounding tissue produces a pattern of local magnetic fields. The protons of water molecules that diffuse within these local fields accumulate a certain phase of the transverse magnetization, which is then collectively detected within the volume of the imaging voxel via a gradient or spin echo (GE and SE), or after a train of refocusing pulses in the case of multiple gradient or spin echoes, or via a balanced steady state free precession (bSSFP) sequence. The dependence of single gradient and spin echoes as a function on the vessel size, vessel orientation, and blood volume fraction has been analyzed and described in several papers (Weisskoff et al., 1994; Boxerman et al., 1995). An open question is the origin of signal formation in bSSFP, which is of crucial importance to interpret the quality of BOLD bSSFP data with respect to the underlying neurovascular point spread function.

This paper focuses on the analysis and description of the neurovascular fingerprint of pass-band bSSFP, an imaging modality that has been introduced for functional BOLD imaging in 2001 (at the stop-band, Scheffler et al., 2001), and that was further advanced by several groups (e.g. Bowen et al., 2005; Miller, 2012; Scheffler and Ehses, 2015). The formation of MR signal from water proton magnetization during a random walk through the neurovascular network is modeled using Monte Carlo simulations for artificial cylinders with different diameter and orientation, as well as for four different sets of neurovascular networks acquired from the mouse parietal cortex measured with two-photon laser scanning microscopy at 1 μm isotropic resolution (Blinder et al., 2013). In addition, selected Monte Carlo simulations of GE and SE have been performed to serve as a comparison to pass band bSSFP.

2. Models and simulations

2.1. Vascular model of the cortex

The underlying vascular structure for Monte Carlo simulations is based on cylinders with different diameter, blood volume (BV) fraction and orientation to the main magnetic field B_0, as well as on four vectorized vessel data sets of the mice parietal cortex that was acquired in a different study by Blinder et al. (2013). In this study, the brains of adult mice were perfused for a fluorescent gel that preserved the volume of vessels. Approximately 1 mm^3 regions of primary vibrissa cortex, from the pia down to the white matter, were isolated and automated optical sectioned with 1 μm resolution. The resultant fluorescence was transformed into interconnected microvessels by matched filtering against cylindrical segments; corrections were made for breaks in the labeling (Kaufhold et al., 2012). Finally, the fully reconstructed image was transformed into an annotated graph, where vessels are branches with a length and median width. Spatial and temporal changes in the local blood oxygenation, blood volume and flow have not been included both for the models based on the artificial cylinders and for the realistic neurovascular data sets. This represents an instantaneous change of blood oxygenation in all vessels. Thus, all vessels structures were either set to a nearly oxygenated state, i.e., a small susceptibility difference between vessels and tissue mimicking the activated state, or to a partially deoxygenated state for the resting state condition.

2.2. Monte Carlo simulations

Monte Carlo simulations closely followed the recipes given by Boxermann et al. (1995); Weisskoff et al. (1994) and Bieri and Scheffler (2007). The susceptibility difference between blood and tissue for fully deoxygenated blood was set to $\Delta\chi = 0.11$ ppm in cgs units, based on a hematocrit level of 40% and a susceptibility difference of fully deoxygenated red blood cells to tissue of $\Delta\chi = 0.273$ ppm (Spees et al., 2001; Jain et al., 2012). A blood oxygenation level of Y = 77% for the resting state was assumed and Y = 85% for the fully oxygenated state (Vovenko, 1999; Gagnon et al., 2015). Applying a field strength of $B_0 = 9.4$T, a cylinder filled with Y = 77% oxygenated blood and oriented perpendicular to B_0 induces in a frequency shift of ±64 Hz at the cylinder surface and 21 Hz within the cylinder, according to the formula shown below (Chu et al., 1990).

$$\Delta\omega(\vec{r}) = 2\pi\gamma B_0(1-Y)\Delta\chi\cdot\frac{R^2}{r^2}\cdot\cos 2\,\phi\cdot\sin^2\theta, \quad r > R \tag{1}$$

$$\Delta\omega(\vec{r}) = 2\pi\gamma B_0(1-Y)\Delta\chi\cdot\left(\cos^2\theta - \frac{1}{3}\right), \quad r \le R \tag{2}$$

R is the cylinder radius and r is the distance between the spin and the central axis of the cylinder. The cylinder is at an angle θ with respect to B_0, and ϕ is the polar angle of the vector r in the plane perpendicular to the cylinder axis.

Similarly to the cylinders, a susceptibility difference Δχ of (1-Y) x 0.11 ppm was assigned to all vessels from the data sets of the parietal cortex of the mice. For simplicity, only the resting state using Y = 80% (Δχ of 0.022 ppm) was compared to the activated, fully oxygenated state with Y = 100% (Δχ = 0 ppm, resulting in a completely homogeneous field within the vessel network). The Finite Perturber Method was used to calculate the resulting frequency map (for a field strength of 9.4T) generated by the vessel models (Pathak et al., 2008; Jenkinson et al., 2004). This method applies a 3D Fourier transform to both the structural data and the field distortion produced by a single finite perturber (sphere). The resulting Fourier-transformed maps are then multiplied and back Fourier-transformed to derive the final frequency distribution of the vessel network oriented at different angles to B_0 (0°–90°).

Random walks of protons were calculated with a diffusion constant of $D = 1.0\ \mu m^2/ms$ and time steps of $\delta t = 50$ μs. For the simulation of the GE signal, an echo time TE of 20 ms was used and 1×10^5 random walks were averaged. For the simulation of the SE signal, an echo time TE of 30 ms was used and 2×10^5 random walks were averaged. The choice of TE = 20 ms versus 30 ms for GE versus SE roughly corresponds to the values used for fMRI at 9.4T (Budde et al., 2014a, 2014b). Pass-band bSSFP was simulated for different TEs, or repetition times TR = 2*TE, ranging from 5 to 20 ms with flip angles between 5° and 30° (using 180° phase cycling), and averaging between 5×10^3 and 1×10^4 random walks. Depending on the selected TR, the bSSFP signal was taken after 500 to 2,500 dummy excitations to ensure a steady state signal. The fractional BV was varied between 1% and 5% for the artificial cylinders, and was between 0.7% and 5% for the measured vessel data sets. The contribution of intra- and extravascular protons was calculated separately, and the overall BOLD signal change is calculated as BV-weighted sum of these contributions. Diffusion of water protons through the vessel-tissue boundary was prohibited.

2.3. Relaxation times

In addition to dephasing effects produced by the inhomogeneous fields, signal changes are heavily dependent on the relaxation times of tissue and the times of oxygenated (active state) or partially deoxygenated (resting state) blood. The chosen relaxation times for tissue and blood strongly influence the resulting signal changes, especially for bSSFP but to a lesser extent for the GE and SE signals.

Relaxation times are closely related to the field strength. This has a significant impact on the relation of intra- and extravascular contributions. In particular, while intra- and extravascular T1 relaxation times are relevant for bSSFP simulations, as both T1 and T2 contribute to the steady state signal, T1 does not contribute to single-echo GE or SE signals. We followed to literature vales (summarized in Fig. 2 in Khajehim and Nasiraei Moghaddam (2017)) and set both intra- and extravascular T1 to 2200 ms for 9.4T. Furthermore, no dependence of intravascular T1 on blood oxygenation was assumed (Blockley et al., 2008). As the steady state signal of bSSFP is approximately proportional to $\sqrt{(T2/T1)}$ (Sekihara K., 1987) and T2 is much smaller than T1, 10–40 ms versus 2200 ms (see below), possible variations of T1 with blood oxygenation will hardly

influence the results of the Monte Carlo simulations. In contrast, selection of appropriate T2 and T2* relaxation times is critical for both GE and SE, and also for bSSFP. In addition, for blood these relaxation times are closely linked to the oxygenation level Y and thus strongly control the intravascular contribution to the overall signal change. Currently there is no experimental data available for T2* of blood at 9.4T. For GE simulations we thus took the experimental data from 1.5 T, 3 T and 7 T (Blockley et al., 2008), and extrapolated the R2* relaxivity to 90 s^{-1} per mM deoxyhemoglobin at 9.4 T. For oxygenation levels of 77% (rest) and 85% (activated), this corresponds to T2* relaxation times of about 4 ms and 8 ms, respectively.

For GE, SE and bSSFP, T2 of the extravascular space was set to 41 ms (Uludağ et al., 2009). As the signal decay in extravascular space is mainly driven by dephasing effects within the inhomogeneous fields around the vessels, the choice of T2 is not critical. For SE with a single echo, a T2 of blood of 12 ms (Y = 77%) and 20 ms (Y = 85%) was used (Uludağ et al., 2009). In the case of rapidly refocused bSSFP or trains of spin echoes, T2 also depends on the refocusing interval, and becomes longer with shorter TR (Dharmakumar et al., 2005; Kurz et al., 2016; Gardener et al., 2010; Grgac et al., 2017). As currently no T2 data of blood with rapid bSSFP refocusing is available, multiple values for the relaxation time T2 were compared in Monte Carlo simulations, i.e., T2 for Y = 77% of 12 ms (corresponding to T2 of a single echo) and 20 ms (narrowing by rapid refocusing), and 20 ms (single echo) and 40 ms (rapid refocusing) for Y = 85%. This choice of T2 for Y = 77% of 12 and 20 ms, and T2 for Y = 85% of 20 and 40 ms roughly corresponds to estimations from literature performed under slightly different conditions (Khajehim and Nasiraei Moghaddam, 2017; Dharmakumar et al., 2005). However, no significant differences of intravascular contributions in bSSFP between the T2 pairs of 12 and 20 ms (rest) and 20 and 40 ms (activated) have been observed. Therefore, all bSSFP simulations shown below are based on a blood T2 of 12 ms at rest (Y = 77%), and 20 ms for activation (Y = 85%).

All BOLD-related signal changes shown in Figs. 1–4, 7 and 8 are relative signal changes in percent of $(S_{Y=85\%}\text{-}S_{Y=77\%})/S_{Y=85\%}$ separately for intra- and extravascular or combined signal contributions. An overview of the parameters used for Monte Carlo simulations are given in Table 1.

2.4. In vivo measurements

A high-resolution functional pass-band bSSFP experiment was performed at 9.4 T on a healthy volunteer with approval by the local ethics committee. The parameters of the 3D bSSFP protocol were as follows: TR = 4.2 ms, TE = 2.1 ms, nominal FA = 15°, resolution = 0.6 × 0.6 × 0.6 mm^3, 16 slices. To accelerate imaging, GRAPPA R = 3 acceleration was used in combination with 5/8 partial Fourier (POCS reconstruction) and elliptical scanning. This resulted in a volume TR of 3.76 s (Scheffler and Ehses, 2015a,b). A flickering radial checker-board was used as a visual stimulus (7 Hz), which was presented for 9 min in alternating 13 s off- and 20 s on-periods. Functional analysis was performed after motion correction using AFNI (Cox, 1996) with FSL's FEAT (Smith et al., 2004) using standard parameter settings and no spatial smoothing. For comparison and vein detection, a high-resolution T2*-weighted GE reference was acquired with the following sequence parameters: TR = 700 ms, TE = 12 ms, nominal FA = 70°, resolution = 0.4 × 0.4 × 0.7 mm^3, 40 slices.

3. Results

We first consider a comparison of the sensitivity to the vessel radius between GE, SE and pass-band bSSFP (Fig. 1). These simulations are based on cylinders at random orientation occupying different BV fractions from 1% to 5%. In accordance with past results (Boxerman et al., 1995; Weisskoff et al., 1994), GE has an unspecific sensitivity to all vessel sizes larger than about 5 μm as a consequence of static dephasing, and a linear dependence of the signal change with BV (Fig. 1a). Similarly, SE shows its typical selectivity to vessel radii between 2 and 10 μm and almost no signal change for larger vessels in the static refocusing regime (Fig. 1b). As for GE, the peak sensitivity in SE scales linearly with the fractional BV. The bSSFP profile is similar to the SE profile (Fig. 1b and c), however, it does not return to zero sensitivity for larger vessels, and has a slightly broader response to the vessel size in accordance to previous work (Bieri and Scheffler, 2007; Kim et al., 2012).

We next consider the dependence of the BOLD bSSFP signal change as a function of different TRs and flip angle (Fig. 2). All simulations show a peak around small vessel radii of about 2–10 μm which slightly varies with the chosen TR. With increasing TR (Fig. 2a–c) the vessel size selectivity shifts to larger radii and the peak signal change is strongly increased, i.e., by a factor of 3–4 going from TR = 5 ms to 20 ms. Also, for longer TR, greater than approximately 10 ms, the contribution from larger vessels (>100 μm) increases to up to 50% of the peak signal. The BOLD-related signal change increases with flip angle up to about 20° by a factor of about 2–3, and shows no further increase for higher flip angles (Fig. 2d–f).

The intra- and extravascular signal contribution as a function of BV, for vessel radii between 2 and 100 μm, was calculated for GE, SE and bSSFP (Fig. 3). For GE, where a blood T2* of 4 ms (resting state Y = 77%) and 8 ms (activated state Y = 85%) at 9.4T was assumed, the intravascular contribution is negligible for all BV and vessel radii (Fig. 3a). Similarly, for SE with blood T2 of 12 ms and 20 ms the intravascular contribution is small compared to the extravascular contribution for vessel radii between 2 and 12 μm (Fig. 3b). However, the extravascular SE signal drops for larger vessel radii and is comparable to the intravascular signal change for vessels radii between 20 and 100 μm. In bSSFP, the relation between intra and extra vascular contribution is similar to SE for small vessels between 2 and 20 μm, so it is mainly dominated by extravascular contributions (Fig. 3c). As the BOLD signal change for bSSFP at vessel radii larger than 50 μm does not completely disappear (but in SE; Fig. 1), intra- and extravascular contributions become comparable at this domain.

The images in Fig. 3d show the response in the visual cortex upon checker board simulation with a T2*-weighted GE image (top) and functional activation in a 0.6 mm isotropic resolution bSSFP acquisition (bottom) with TR = 4.2 ms and nominal flip angle of 15°. The small vein penetrating into the cortex shows a strong BOLD response. The BV of pixels close or within this vein is close to 100%, and thus the signal change is only produced by the intravascular signal. This signal change only depends on the T2 change of blood from 12 ms (rest) to 20 ms (activated), and as the bSSFP signal is proportional to about $\sqrt{(T2/T1)}$ this change is in the range of 20–50%.

In Fig. 4, only parallel cylinders with a certain angle to B_0 have been

Table 1
Summary of parameters used in Monte Carlo simulations. Rest/Act refers to the resting/activated state with different oxygenation levels Y_{rest}/Y_{act}.

	Y_{rest}	Y_{act}	Vessel radius	Blood volume	TR for bSSFP	Flip angle for bSSFP	Blood T1/T2 for bSSFP	Blood T1/T2 for SE	Blood T1/T2* for GE	Extra-vascular T1/T2
Random/parallel cylinders	77%	85%	0.5–200 μm	1%–5%	5 -20 ms	5°–30°	Rest: 2,200/ 12 ms	Rest: 2,200/ 12 ms	Rest: 2,200/ 4 ms	2,200/41 ms
Vessel data	80%	100%	1.0–40 μm	0.1%–5%	5 ms	20°	Act: 2,200/20 ms	Act: 2,200/ 20 ms	Act: 2,200/ 8 ms	

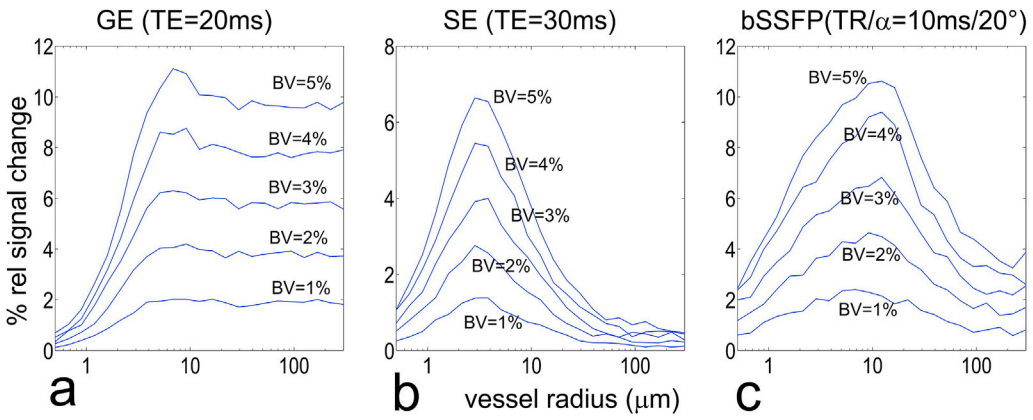

Fig. 1. Total BOLD signal change of GE, SE and bSSFP as a function of vessel radius (randomly oriented cylinders) for different fractional BV. Blood oxygenation of Y = 77% and Y = 85% was assumed for the resting and activated state, respectively, at a field strength of 9.4T.

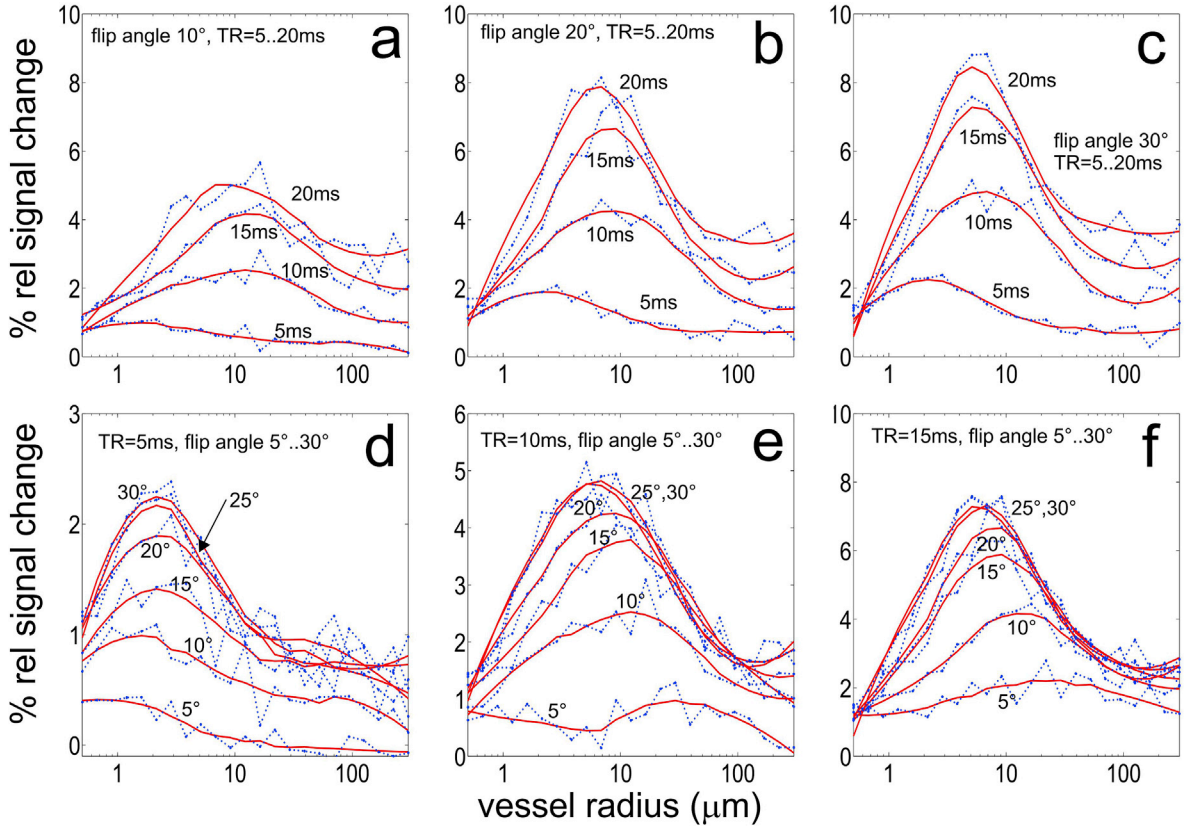

Fig. 2. Extravascular BOLD signal change for bSSFP for different TR and flip angles as a function of the vessel radius (red lines are polynomial fits to the simulation results (in blue)). Blood oxygenation of Y = 77% and Y = 85% was assumed for the resting and activated state, respectively, at a field strength of 9.4T. Intravascular blood T2 was set to T2 = 12 ms for the resting state and T2 = 20 ms for the activated state. The fractional BV of the randomly oriented cylinders was set to 2% for all simulations.

simulated. This mimics a very simplified model of parallel diving (penetrating) veins and arteries oriented perpendicular to the cortical surface. For GE, basically all vessel radii exhibit a strong dependence of the signal change on the cylinder orientation to B_0. For bSSFP simulated at TR = 5 ms, only small vessels (1–10 μm) depend on their angle to B_0, larger vessels just give a very small signal change, which is similar to the SE behavior shown right. As the bSSFP sensitivity to larger vessels increases with TR (see Fig. 2), the bSSFP simulation using TR = 15 ms shows some signal dependence on orientation to B_0 also for larger vessels around 50–200 μm.

Fig. 5 summarizes the distribution of vessel length, the orientation angle of vessels to the surface normale and the diameter and tortuosity, calculated from the vessel data sets (Blinder et al., 2013). Both venules and arterioles are mostly oriented parallel to the surface normal. However, due to the curvilinear nature of the cortical surface, the vertical axis of the dataset did not always locally match the surface perpendicular. We quantify the average offset of the local surface norm from the vertical axis of the dataset to be 6.2 ± 3.1°. Regarding capillary orientation, the data show a clear bias to be perpendicular to the normal.

Simulations based on reconstructed cortical neurovascular network were performed by dividing each network into six equally spaced layers starting from the top showing the large cortical surface vessels (layer 1) down to the boundary of grey and white matter (layer 6) (right panels, Fig. 6A–D). The Larmor frequency distribution within the layers was

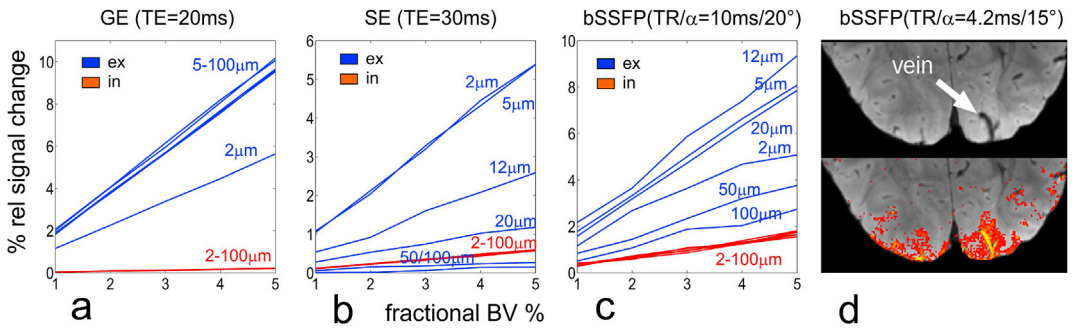

Fig. 3. Relation between intra- (red) and extravascular (blue) contribution for GE, SE and bSSFP based on randomly oriented cylinders as a function of fractional BV and for radii varying from 2 to 100 μm. Blood T2* was set to T2* = 4 ms and 8 ms for GE, T2 = 12 ms and 20 ms for SE and bSSFP for the resting and activated state, respectively. The image on the right top shows a GE measurement (TE = 12 ms) depicting a larger vein (white arrow). Below is a functional activation map (visual checkerboard stimulation, 0.6 mm isotropic resolution) overlaid onto the GE image. The strong intravascular signal from a draining vein is clearly visible.

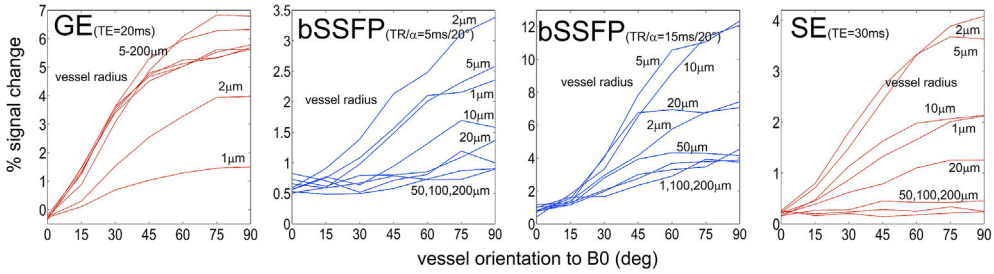

Fig. 4. Total BOLD signal change as a function of the orientation of the vessel (cylinder) to B_0 for GE, bSSFP and SE for different vessel radii ranging from 1 to 200 μm, and for a fractional BV of 2%.

calculated by the Finite Perturber Method. As layer 1 includes the large cortical surface vessels, the corresponding frequency distribution is much broader compared to deeper layers (left panels, Fig. 6A–D). However, the layer-specific frequency distributions show a large variation across the four different data sets. The width of the frequency distribution for layers 2 to 6 varies between ±5 and ± 15 Hz. In addition, the frequency distribution of data sets B, C and D is more symmetric compared to A. The signal changes shown in the right part of Fig. 6 are strongest for the surface layer 1, and they decrease by about a factor of 4–6 for GE and about 2–3 for SE and bSSFP going towards the deeper layers. The simulated functional signal change for GE (TE = 20 ms), SE (TE = 30 ms) and bSSFP (TR/α = 5 ms/20°), as well as local fractional BV for each layer, is seen (right panels, Fig. 6A–D). Functional signal changes were calculated for two orientations of the vessel network to B_0, 0° (dotted line, surface perpendicular to B_0) and 90° (solid line, surface parallel to B_0). For GE, a very strong signal change increase can be observed towards the surface layer 1 which is less pronounced for bSSFP and SE. A certain dependence on the orientation to B_0 is visible for all modalities, but is strongest for GE. The effect on orientation is inverted, starting from the surface layer to deeper layers, and occurs since surface vessels are mostly perpendicular to the penetrating vessels.

Fig. 7 shows averaged values across the four data sets shown in Fig. 6, as well as separated extra and intravascular contributions.

The signal change dependence on the orientation of the cortex to B_0 is summarized in Fig. 8. The left column shows renderings of the four vectorized vessel data sets of the mice parietal cortex. The three columns on the right show signal changes for GE (TE = 20 ms), SE (TE = 30 ms) and bSSFP (TR/α = 5 ms/20°) as a function of the orientation to B_0, where for 0° and 180° the penetrating vessels are parallel, and surface vessels are perpendicular to B_0. The calculated signal changes are relative to the change observed at 90° and were calculated in percent by 100 x $(\Delta S_{\theta z}\text{-}\Delta S_{90^\circ})/\Delta S_{90^\circ}$ for each of the six layers and for the mean signal across layers shown in red.

4. Discussion

The presented results are all based on Monte Carlo simulations assuming a certain global oxygenation change between Y = 77% and Y = 85%, and for a field strength of 9.4T. In general, the frequency pattern around cylinders or vessels scales linearly with oxygenation and field strength, and thus the resulting signal change strongly depends on these parameters. However, the basic characteristics of the presented plots, such as the selectivity to a certain vessel radius, the dependence on the fractional BV and the orientational dependence, do not depend on the particular choice of the selected parameters. Similar shapes of signal changes as a function of the vessel size and fractional BV have been reported for GE, SE and bSSFP (Boxerman et al. (1995); Weisskoff et al. (1994); Bieri and Scheffler, 2007; Kim et al., 2012; Khajehim and Nasiraei Moghaddam, 2017). Similarly, the choice of relaxation times of the extra- and intravascular space have an impact on the overall signal changes, and more significantly also on the relation of intra- and extravascular contributions. As far as possible, the selected relaxation times were taken from literature values, or they were extrapolated to 9.4T.

4.1. Specificity to the capillary and non-capillary network

The well-known behavior of GE, SE and pass-band bSSFP as a function of vessel (cylinder) size could be confirmed in Fig. 1. Experimental comparisons between GE and bSSFP in functional checker board experiments at 9.4T, however, show a lower signal change for bSSFP compared to GE (Scheffler and Ehses, 2015a,b), in contrast to signal changes presented in Fig. 1. This might be related to the vessel size selectivity of bSSFP, as larger vessels contribute to GE but less to bSSFP. Compared to SE, bSSFP shows a slightly larger contribution for vessels larger than 50 μm, which can be attributed to the stronger intravascular effect compared to SE, see below.

The shape as well as the peak of the curve that describes the bSSFP signal change as a function of vessel radius depend on TR and flip angle.

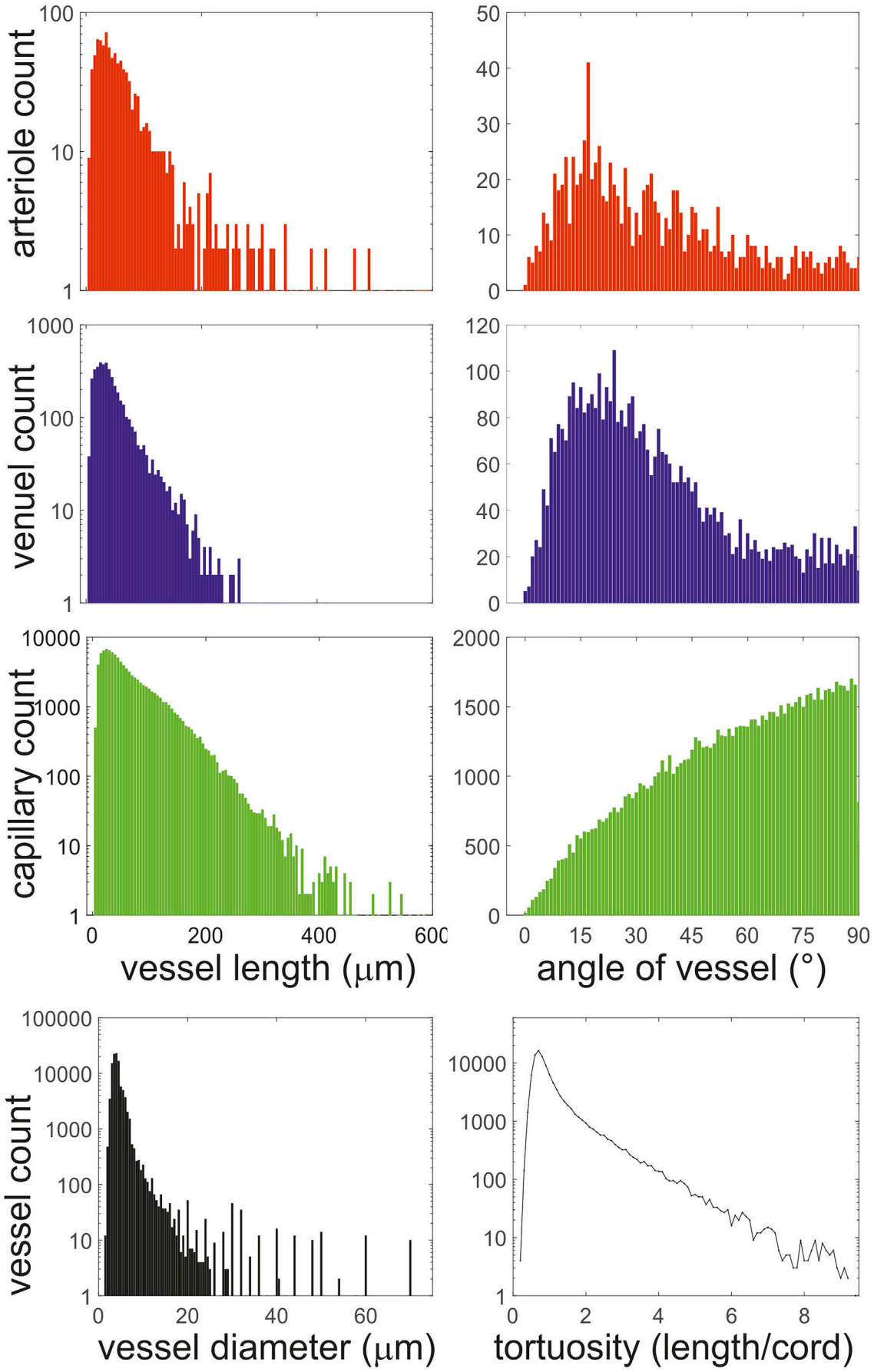

Fig. 5. Top: Vessel length and angle of vessels to the surface normal for arterioles, venules and capillaries (diameter < 7 μm), averaged over the four data sets shown in Fig. 8. Bottom: Distribution of vessel diameter and tortuosity (length divided by the cord (end-to-end length)) for all vessel types.

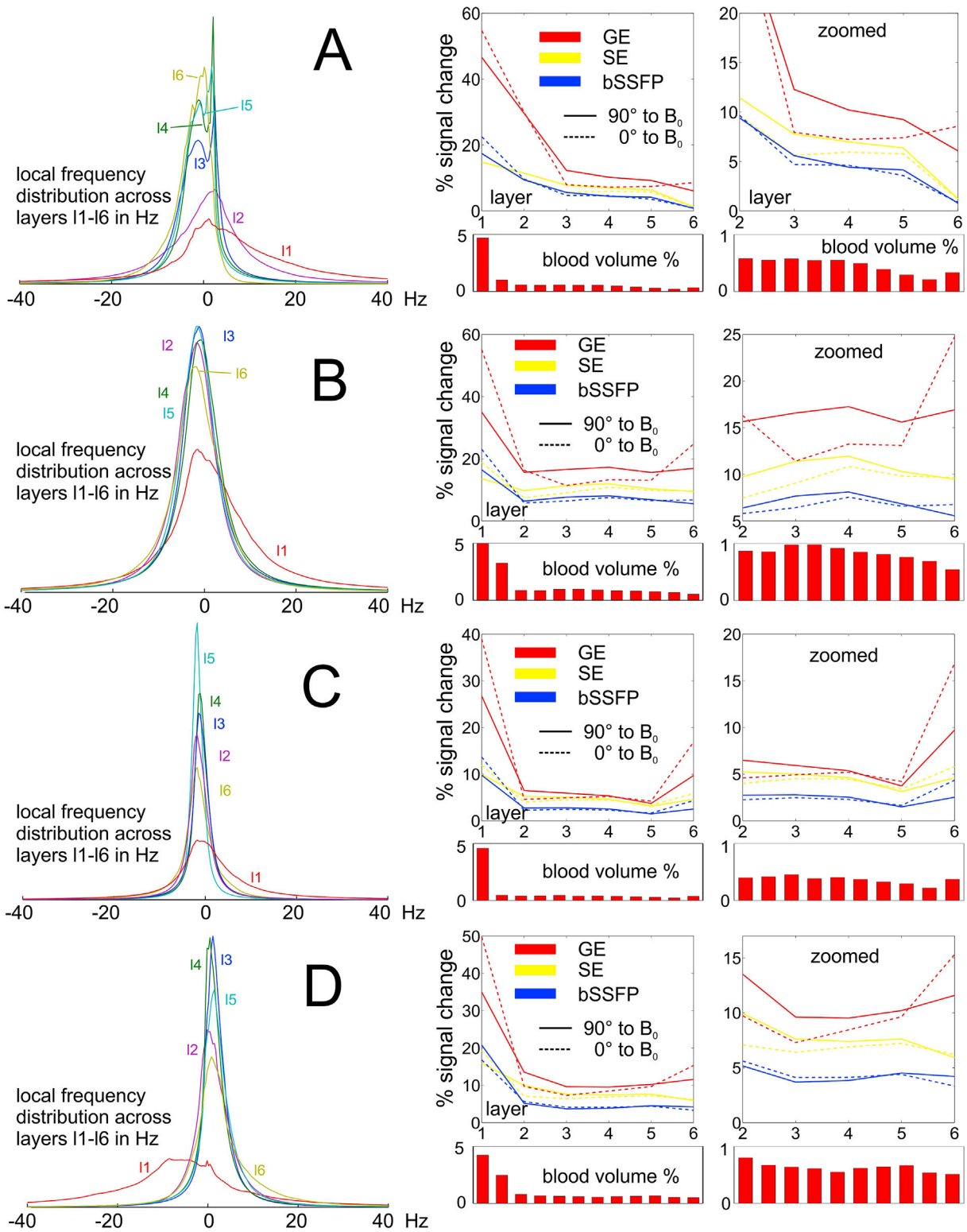

Fig. 6. The left column shows the frequency distribution (assuming $\Delta\chi = 0.22 \times 10^{-7}$ at 9.4T and with the top surface of the vessel network oriented perpendicular to B_0) around the vessel network for layers l1 to l6 for the four different data sets A to D shown in Fig. 6. The middle and right (zoomed for layers l2 to l6) column shows total BOLD signal changes for GE (TE = 20 ms), SE (TE = 30 ms) and bSSFP (TR/α = 5 ms/20°) across layers l1 to l6 oriented perpendicular (0°, dotted line) and parallel (90°, solid line) to B_0. The corresponding fractional BV across layers extracted from the data set is shown below each plot.

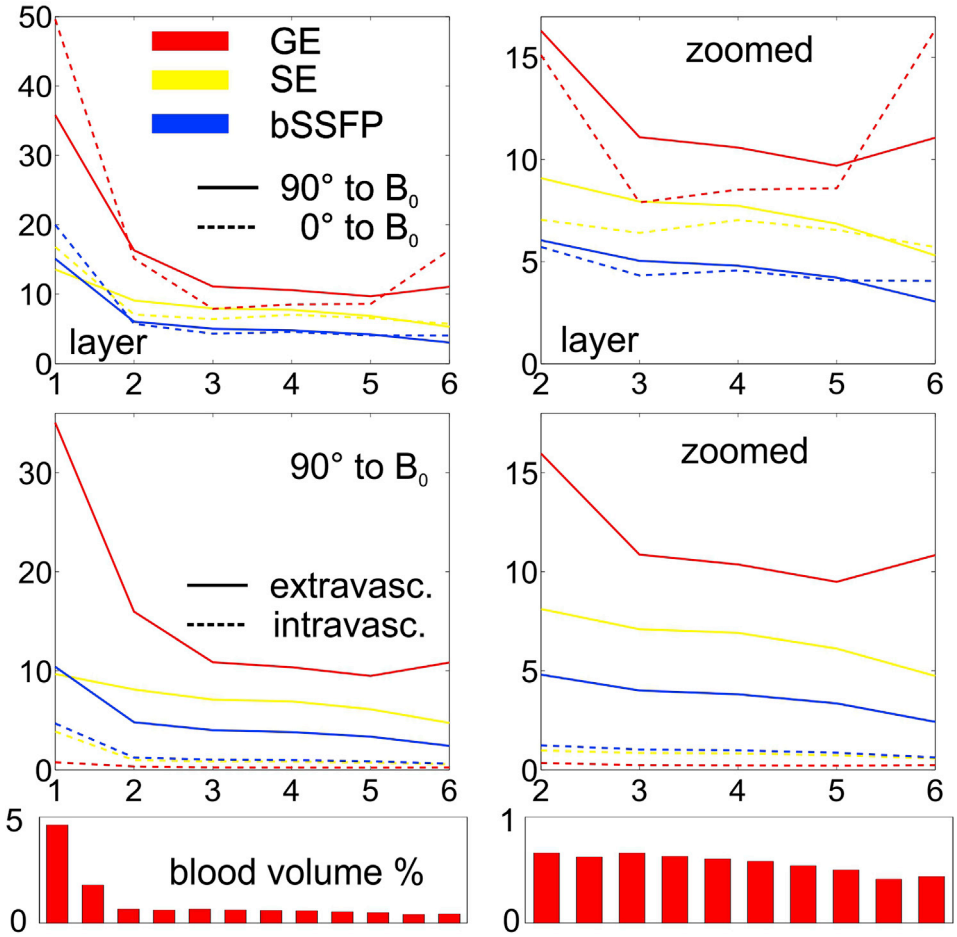

Fig. 7. Top row shows averaged total BOLD changes across the four data sets A to D, corresponding blood volumes are shown in the bottom row. The middle row depicts signal changes separated into extra and intra vascular part. The sum of these changes corresponds to the plots shown in the top row.

The curves shown in Fig. 2 are similar to those shown in other publications that used largely different parameters for their simulations (Bieri and Scheffler, 2007; Kim et al., 2012; Khajehim and Nasiraei Moghaddam, 2017). An increase in TR gives a much higher signal change, and in parallel, an increasingly contribution from larger vessels (>50 μm). An increase of the flip angle to about 20°–25° also boosts the signal change as shown in the bottom row of Fig. 2, similar to the results shown in Kim et al. (2012), Miller and Jezzard (2008) and Khajehim and Nasiraei Moghaddam (2017). The contribution of vessels larger than 50 μm is less pronounced for increasing flip angles (bottom row in Fig. 2) than for increasing TRs (top row). For experimental applications a longer TR of 10–15 ms thus seems to be beneficial. In addition, higher flip angles can be used due to the lower power deposition. A drawback of longer TRs at very high fields is increased banding artifacts.

According to the plots in Figs. 1 and 2, the BOLD signal ratio, which can be defined as the ratio of the contributions from the laminar vasculature and from intracortical veins (Markuerkiaga et al., 2016), is significantly different for GE, SE and bSSFP. Assuming a laminar network that consists of vessels of up to 10 μm and that occupy 2.3% BV (Weber et al., 2008; Boas et al., 2008), and intracortical veins between 10 μm and 70 μm and an averaged BV across layers of 0.6% (from 0.2% at layer 6 linearly increasing to 1.2% at the top layer 1, Cassot et al., 2006; Duvernoy et al., 1981), the BOLD signal ratio (laminar vasculature: intracortical veins) of GE (TE = 20 ms) amounts to 10:1 (layer 6) to 1.7:1 (top layer 1), that of SE (TE = 30 ms) to 34:1 to 6:1, and 22:1 to 4:1 for bSSFP (TR/α = 10 ms/20°). Averaged over the cortex thickness and using a mean intracortical vein BV of 0.6%, the BOLD signal ratio amounts to 3.2:1 for GE, 12:1 for SE, and 7.5:1 for bSSFP. Thus, the BOLD signal ratio, i.e. the selectivity to oxygenation changes in capillaries and venules is highest for SE, followed by bSSFP (depending on TR of bSSFP) and is much lower for GE. However, it should be noted that most functional studies using SE are based on SE-EPI readouts that show a T2* decay around the spin echo that is usually placed in the center of k-space. The resulting T2*-related blurring will thus introduce a certain GE-type weighting, depending on the resolution and acceleration factor. Thus, as bSSFP only acquires one single k-space line per TR, the GE contribution in bSSFP might be comparable or even less compared to SE-EPI.

Furthermore, all sequence show an increased BOLD signal change towards the cortical surface, as shown in Figs. 6 and 7. The frequency distribution around the vessels based on the measured optical data set depends on the layer level. The observed signal change thus depends on the chosen resolution of the functional imaging sequence: if a single voxel covers the entire thickness of the cortex, about 50% of the signal change is produced by surface vessels for GE, but only about 10–20% for SE and bSSFP (assuming an isotropic resolution of 2–3 mm as commonly used in functional studies). Thus, SE and bSSFP capture significantly more responses from deeper layers compared to GE. At higher resolution, however, the BOLD signal ratio becomes more similar across sequences, except for the surface layer 1.

4.2. *Intra-versus and extravascular signals*

The contribution of intra- and extravascular signals for different fractional BV is shown in Fig. 3 for GE, SE and bSSFP, in an experimental example depicting a larger draining vein, as well as in Fig. 7. As mentioned above, diffusion of water between intra- and extravascular

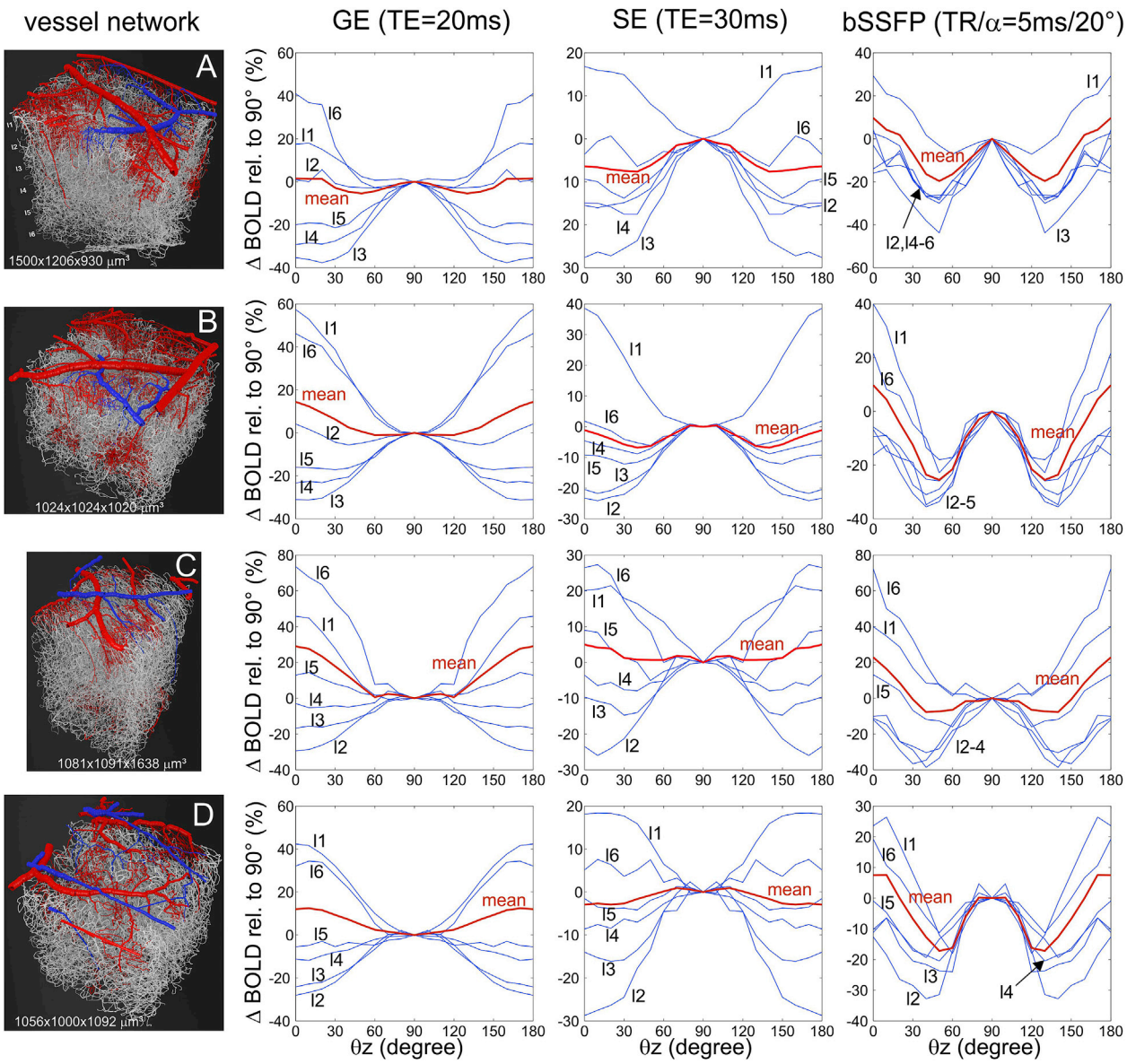

Fig. 8. The left column depicts the rendered vessel data sets used for Monte Carlo simulations. The three right columns show the orientational and layer-specific total BOLD signal change dependence of GE, SE and bSSFP as relative percentage change to the reference at 90° (layer surface parallel to B_0 or penetrating vessels perpendicular to B_0). The red curves are the mean through all layers, i.e. represent the BOLD response of the entire cortical structure. For simplicity, orientations for $\theta > 90°$ were set equal to those of $\theta_{>90°} = 180° - \theta_{<90°}$.

space was prohibited in all simulations. However, allowing water to cross vessel boundaries with a probability of 10% (Eichling et al., 1974; Paulson et al., 1977) does increase the intravascular contribution for all acquisition modalities, and especially for very small vessels. We did not include these data here, but it might offer a method to probe vessel permeability. The results shown in Figs. 3 and 7 strongly depend on the chosen intravascular T2 and T2* relaxation times, which were set to 4 ms and 8 ms for GE, and 12 ms and 20 ms for SE and bSSFP, for the resting and activated state, respectively. Intravascular T2* at 9.4T is very small and thus does not produce a significant intravascular signal for GE, but it increases with lower field strength (Gomori et al., 1987; Silvennoinen et al., 2003; Blockley et al., 2008). GE shows a strong and similar extravascular signal for all vessels larger than 5 µm. For SE only vessels between 2 and 10 µm produce a much stronger extravascular signal compared to vessels larger than 20 µm and to the intravascular signal. BSSFP is somewhat less selective compared to SE: vessels larger than 50 µm produce similar intra- and extravascular signals, smaller vessels are more extravascular-weighted. Thus, the signal characteristic of bSSFP is comparable to that of SE providing a strong signal change only for small vessels. The image on the right in Fig. 3 shows an example of high-resolution functional bSSFP with a huge activation in a vein of about 1 mm diameter. In this case, the fractional BV is almost 100% and the signal is thus solely given by the T2 change of blood. Therefore, in case of very high BV within the voxel, bSSFP gives a strong functional response in contrast to GE for which the strong T2* decay almost completely destroys the signal. However, for BVs below about 5% (which is typical or even smaller for grey matter, except for the surface vessels, see Figs. 6 and 7), bSSFP (as SE) is mostly responsive to capillaries and less sensitive to the larger diving vessels. Significantly different results for the relation of intra- and extravascular contribution have been reported in a Monte Carlo simulation by Fujita (2001) and Kim et al. (2012). Fig. 4 in the Kim paper shows a more than 60% intravascular contribution to the overall signal at 3T, however, the used T2 relaxation times for blood are not explicitly given. The intravascular contribution increases linearly with BV and, for example, contributes to about 1.5% for GE, 7% for SE and 11% for bSSFP to the overall signal change at 9.4T and a BV of 30%, often found in pathological tissue such as brain tumors. In general, the intravascular contribution is larger at lower fields and reduced at larger fields

due to the dependency of T2/T2* on field strength. A comparison of intra and extravascular contribution for different layers is shown in Fig. 7, which was averaged across the four data sets. The strong increase in signal change at the surface or layer 1 can be observed for all sequences. However, for GE this increase is mainly produced by extravascular contributions. For SE and bSSFP this increase is induced roughly equally by both compartments.

4.3. Orientational bias

The dependence of the signal change on the orientation of the cortex to B_0 clearly demonstrates, that the vessel structure is highly oriented and far from being a randomly oriented set of cylinders. A periodic dependence can be observed in all plots shown on the right-hand side in Fig. 8 across all layers, and also a phase or angle shift of 90° between layers 1, 6 and layers 2–5. This indicates that vessel orientations between these layers are perpendicular to each other. Furthermore, there seems to be a striking difference of the orientational signal dependence in bSSFP compared to GE and SE: while the angular signal dependence in GE and SE mostly shows one period of signal changes within 0°–180°, the bSSFP response for single layers as well as for the mean across layers seems to be slightly bi-periodic. This is also partially the case for SE but only for the mean response. Based on Fig. 4 this might be explained by the fact that even for small vessels in the range of 1–20 μm the vessel network is not randomly oriented but has a vessel structure that is partially oriented perpendicular to each other, such as capillaries that branch perpendicular to the diving or ascending vessels. Such structures have been presented for example in Gagnon et al. (2015), Weber et al. (2008) and Blinder et al. (2013). However, it remains open if this bi-periodic behavior can be generalized to different cortical areas or even to humans, or subcortical vessel networks. A similar, mono-periodic dependence has been reported by Gagnon et al. (2015) and Fracasso et al. (2017) and Kurz et al. (2017) based both on experiments and Monte Carlo simulations. However, these data show a much stronger angular dependence for GE compared to SE (bSSFP was not analyzed there). In our simulations all sequences show an angular dependence for both single layers and mean signals, however, to a lesser extend for SE compared to GE, and largest and bi-periodic for bSSFP. The dependence of the signal change on the orientation of the cortex to B_0 has implications for any quantitative or calibrated measurement of oxygenation changes or contrast agent-induced susceptibility changes as used, for example, in first-pass contrast-enhanced perfusion measurements. The derived results of such studies might be strongly biased by the local orientation of the cortex to B_0, and we are thus currently starting experiments with blood pool SPIO contrast agents to precisely describe and quantify these effects for different field strengths, resolution, and sequence types.

4.4. Limitations of this study

In general, a limitation of this study is the simplified assumption of a certain susceptibility difference between all vessels types and surrounding tissues without any dynamic and spatially varying patterns of oxygenation and blood volume changes. Therefore, our results do not contribute to the question, whether layer-specific neuronal activation can be detected with GE, SE or bSSFP. As shown in Figs. 6 and 7, a prerequisite for layer-specific activation is a sufficiently high spatial resolution, as otherwise the major response is induced by surface vessels, especially for GE. However, disentangling responses from different layers probably requires a detailed knowledge of the spatially resolved oxygenation and blood volume dynamics. Some excellent examples of these dynamic changes of oxygenation and flow based on optical methods are shown in Boas et al. (2008), Gagnon et al. (2015) and Schmid et al. (2017). As these oxygenation patterns rapidly propagate through the cortex within fractions of seconds, only a very rapid fMRI method with very high resolution might be able to capture these layer-specific changes.

Furthermore, the BOLD signal characteristics of GE, SE and bSSFP shown in Figs. 6–8 are related to the vessel architecture of the mouse parietal cortex. An analysis of other cortical or subcortical regions in animals or humans would be of high interest, however, to our knowledge currently no such high-resolution data is available. Another critical parameter is diffusion of water across the vessel boundary at high fields. The very short T2 or T2* of blood together with diffusion into and out of the vessels act as a relaxation mechanism. In our simulation we assumed non-permeable vessels, but according to literature there is a small diffusion permeability coefficient for water passage across the blood brain barrier of about 2×10^{-6} m/s (Eichling et al., 1974; Paulson et al., 1977). This increases the BOLD signal change especially for larger vessels (20–200 μm) in SE and bSSFP and thus reduces the selectivity to smaller vessels.

5. Conclusion

The main reason to choose ultra-high field is the relatively low sensitivity of bSSFP to BOLD changes at much lower fields, and pass-band bSSFP is thus probably not a good candidate for fMRI at 1.5T and 3T compared to GE. At higher fields of 7T or more, bSSFP provides a sensitivity that is almost comparable to SE (Scheffler and Ehses, 2015a,b) and thus represents an alternative method to fMRI compared to GE with the advantage of being more selective to the microvasculature. Furthermore, application of SE-EPI at ultra-high fields is limited by SAR constrains, whereas full brain coverage with bSSFP is feasible even at 9.4T. At 9.4T, the intravascular contribution is negligible for GE, and depending on the BV, increases to about 5%–10% of the overall BOLD signal change for SE and bSSFP. Except for larger veins that occupy a huge volume fraction of the imaging voxel, bSSFP is mostly sensitive to extravascular contributions from small vessels. The BOLD signal ratio between microvessels and intracortical veins is highest for deep layers (about 20:1) and decreases to about 4:1 for the surface layer for bSSFP. Thus, the contribution of larger cortical veins is in the range of 5%–20%, indicating a strong sensitivity of bSSFP to the microvasculature. All sequences show a strong dependence on the orientation of the cortical layers to B_0 due to perpendicularly arranged feeding and draining vessels. Especially for SE and bSSFP, this observation needs to be confirmed in further, experimental studies, but it might have a significant impact on any quantitative or calibrated BOLD or perfusion measurements.

Acknowledgement

Mario Gilberto Báez-Yánez is thankful for the support by CONACYT (Consejo Nacional de Ciencia y Tecnología, México), and we also thank the NIH-NINDS (grant R35NS097265) and the NIH-NIMH (1R01MH111438) for funding.

References

Bieri, O., Scheffler, K., 2007. Effect of diffusion in inhomogeneous magnetic fields on balanced steady-state free precession. NMR Biomed. 20, 1–10.
Blinder, P., et al., 2013. The cortical angiome: an interconnected vascular network with noncolumnar patterns of blood flow. Nat. Neurosci. 15 (7), 889–897.
Blockley, N.P., et al., 2008. Field strength dependence of R1 and R*2 relaxivities of human whole blood to ProHance, vasovist, and deoxyhemoglobin. Magn. Reson. Med. 60, 1313–1320.
Boas, D.A., et al., 2008. A vascular anatomical network model of the spatio-temporal response to brain activation. NeuroImage 40 (3), 1116–1129.
Bowen, C.V., et al., 2005. High field balanced-SSFP FMRI: a BOLD technique with excellent tissue sensitivity and superior large vessel suppression. Miami. In: Proc 13th ISMRM, p. 119.
Boxerman, J.L., et al., 1995. MR contrast due to intravascular magnetic-susceptibility perturbations. Magn. Reson. Med. 34, 555–566.
Budde, J., et al., 2014a. Functional MRI in human subjects with gradient-echo and spin-echo EPI at 9.4 T. Magn. Reson Med. 71 (1), 209–218.
Budde, J., et al., 2014b. Ultra-high resolution imaging of the human brain using acquisition-weighted imaging at 9.4T. Neuroimage 1 (86), 592–598.

Cassot, F., et al., 2006. A novel three-dimensional computer-assisted method for a quantitative study of microvascular networks of the human cerebral cortex. New York, N.Y.: 1994 Microcirculation 13 (1), 1–18.
Chu, S., et al., 1990. Bulk magnetic susceptibility shifts in NMR studies of compartmentalized samples: use of paramagnetic reagents. Magn. Reson. Med. 13, 239–262.
Cox, R.W., 1996. AFNI: software for analysis and visualization of functional magnetic resonance neuroimages. Comput. Biomed. Res. 29 (3), 162–173.
Deistung, A., et al., 2013. High-resolution MR imaging of the human brainstem in vivo at 7 tesla. Front. Hum. Neurosci. 7, 710.
Dharmakumar, R., et al., 2005. Oxygen-sensitive contrast in blood for steady-state free precession imaging. Magn. Reson. Med. 53, 574–583.
Duvernoy, H.M., et al., 1981. Cortical blood vessels of the human brain. Brain Res. Bull. 7 (5), 519–579.
Eichling, J.O., et al., 1974. Evidence of the limitations of water as a freely diffusible tracer in brain of the rhesus monkey. Circ. Res. 35 (3), 358–364.
Federau, C., Gallichan, D., 2016. Motion-correction enabled ultra-high resolution in-vivo 7t-mri of the brain. PLoS ONE 11 (5), e0154974.
Fracasso, A., et al., 2017. Laminar imaging of positive and negative BOLD in human visual cortex at 7T. pii: S1053–8119 Neuroimage 17, 30149-0, 10.1016.
Fujita, N., 2001. Extravascular contribution of blood oxygenation level-dependent signal changes: a numerical analysis based on a vascular network model. Magn. Reson. Med. 46, 723–734.
Gagnon, L., et al., 2015. Quantifying the microvascular origin of BOLD-fMRI from first principles with two-photon microscopy and an oxygen-sensitive nanoprobe. J. Neurosci. 35 (8), 3663–3675.
Gardener, A.G., et al., 2010. Dependence of blood R2 relaxivity on CPMG echo-spacing at 2.35 and 7 T. Magn. Reson. Med. 64, 967–974.
Gomori, J.M., et al., 1987. NMR relaxation times of blood: dependence on field strength, oxidation state, and cell integrity. J. Comput. Assist. Tomogr. 11, 684–690.
Grgac, K., Li, W., Huang, A., Qin, Q., van Zijl, P.C., et al., 2017. Transverse water relaxation in whole blood and erythrocytes at 3T, 7T, 9.4T, 11.7T and 16.4T; determination of intracellular hemoglobin and extracellular albumin relaxivities. Magn. Reson Imaging 38, 234, 24.
Jain, V., et al., 2012. Investigating the magnetic susceptibility properties of fresh human blood for noninvasive oxygen saturation quantification. Magn. Reson. Med. 68 (3), 863–867.
Jenkinson, M., et al., 2004. Perturbation method for magnetic field calculations of nonconductive objects. Magn. Reson. Med. 52, 471–477.
Kaufhold, J.P., et al., 2012. Vectorization of optically sectioned brain microvasculature: learning aids completion of vascular graphs by connecting gaps and deleting open-ended segments. Med. Image Anal. 16 (6), 1241–1258.
Keuken, M.C., et al., 2013. Ultra-high 7T MRI of structural age-related changes of the subthalamic nucleus. J. Neurosci. 33 (11), 4896–4900.
Khajehim, M., Nasiraei Moghaddam, A., 2017. Investigating the spatial specificity of S2-SSFP fMRI: a Monte Carlo simulation approach. Magn. Reson Imaging 37, 282–289.
Kim, T.S., et al., 2012. Analysis of the BOLD characteristics in pass-band bSSFP fMRI. Int. J. Imaging Syst. Technol. 22 (1), 23–32.
Kurz, F.T., et al., 2016. CPMG relaxation rate dispersion in dipole fields around capillaries. Magn. Reson. Imaging 34, 875–888.
Kurz, F.T., et al., 2017. The influence of spatial patterns of capillary networks on transverse relaxation. Magn. Reson. Imaging 40, 31–47.
Lüsebrink, F., et al., 2017. T1-weighted in vivo human whole brain MRI dataset with an ultrahigh isotropic resolution of 250 μm. Sci. Data 14 (4), 170032.
Markuerkiaga, I., et al., 2016. A cortical vascular model for examining the specificity of the laminar BOLD signal. NeuroImage 132, 491–498.
Miller, K.L., 2012. FMRI using balanced steady-state free precession (SSFP). NeuroImage 62, 713–719.
Miller, K.L., Jezzard, P., 2008. Modeling SSFP functional MRI contrast in the brain. Magn. Reson. Med. 60, 661–673.
Murphy, K., et al., 2013. Resting-state fMRI confounds and cleanup. Neuroimage 80, 349–359.
Ocali, O., Atalar, E., 1998. Ultimate intrinsic signal-to-noise ratio in MRI. Magn. Reson Med. 39, 462–473.
Pathak, A.P., et al., 2008. A novel technique for modeling susceptibility-based contrast mechanisms for arbitrary microvascular geometries: the finite perturber method. NeuroImage 40, 1130–1143.
Paulson, O.B., et al., 1977. Filtration and diffusion of water across the blood-brain barrier in man. Microvasc. Res. 13 (1), 113–124.
Pohmann, R., et al., 2016. Signal-to-noise ratio and MR tissue parameters in human brain imaging at 3, 7, and 9.4 tesla using current receive coil arrays. Magn. Reson Med. 75 (2), 801–809.
Scheffler, K., Ehses, P., 2015a. High-resolution mapping of neuronal activation with balanced SSFP at 9.4 tesla. Magn. Reson. Med. 76, 163–171.
Scheffler, K., Ehses, P., 2015b. High-resolution functional imaging in the human brain using passband bSSFP at 9.4T. In: Proc 23th ISMRM, p. 2076. Toronto.
Scheffler, K., et al., 2001. Detection of BOLD changes by means of frequency-sensitive TrueFISP technique: preliminary results. NMR Biomed. 14, 1–7.
Schmid, F., et al., 2017. Depth-dependent flow and pressure characteristics in cortical microvascular networks. PLoS Comput. Biol. 13 (2), e1005392.
Sekihara, K., 1987. Steady-state magnetizations in rapid NMR imaging using small flip angles and short repetition intervals. IEEE Trans. Med. Imaging 6, 157–164.
Silvennoinen, M.J., et al., 2003. Comparison of the dependence of blood R2 and R2* on oxygen saturation at 1.5 and 4.7 Tesla. Magn. Reson Med. 49, 47–60.
Smith, S.M., et al., 2004. Advances in functional and structural MR image analysis and implementation as FSL. NeuroImage 23 (1), S208–S219.
Spees, W.M., et al., 2001. MR properties of human blood at 1.5 Tesla. T1, T2, T2* and Gaussian relaxation behavior. Magn. Reson. Med. 45, 533–542.
Uludağ, K., et al., 2009. An integrative model for neuronal activity induced signal changes for gradient and spin echo functional imaging. NeuroImage 48 (1), 150–165.
Vovenko, E., 1999. Distribution of oxygen tension on the surface of arterioles, capillaries and venules of brain cortex and in tissue in normoxia: an experimental study on rats. Pflugers Arch. 437 (4), 617–623.
Weber, B., et al., 2008. The microvascular system of the striate and extrastriate visual cortex of the macaque. Cereb. Cortex 18 (10), 2318–2330.
Weisskoff, R., et al., 1994. Microscopic susceptibility variation and transverse relaxation: theory and experiment. Magn. Reson. Med. 31, 601–610.
Wiesinger, F., et al., 2004. Electrodynamics and ultimate SNR in parallel MR imaging. Magn. Reson Med. 52, 376–390.